mater.scichina.com link.springer.com

Published online 17 March 2022 | https://doi.org/10.1007/s40843-022-1986-5
*Sci China Mater* 2022, 65(8): 2289–2297

SPECIAL ISSUE: Flexible Intelligent Materials

# Stress-deconcentrated ultrasensitive strain sensor with hydrogen-bonding-tuned fracture resilience for robust biomechanical monitoring

Yizhuo Yang[1†], Wenjie Tang[1†], Jinyi Wang[1,2†], Ruiqing Liu[1], Ping Yang[3], Shisheng Chen[1], Yuehui Yuan[1], Jingfeng Xu[1], Xueyang Ren[1], Shancheng Yu[1], Hao Wu[1], Yunfan Zhou[4], Leili Zhai[4], Xiaodong Shao[4], Zenan Chen[1] and Benhui Hu[1,4,5*]

**ABSTRACT Recently, rapid advances in flexible strain sensors have broadened their application scenario in monitoring of various mechanophysiological signals. Among various strain sensors, the crack-based strain sensors have drawn increasing attention in monitoring subtle mechanical deformation due to their high sensitivity. However, early generation and rapid propagation of cracks in the conductive sensing layer result in a narrow working range, limiting their application in monitoring large biomechanical signals. Herein, we developed a stress-deconcentrated ultrasensitive strain (SDUS) sensor with ultrahigh sensitivity (gauge factor up to 2.3 × $10^6$) and a wide working range (0%–50%) *via* incorporating notch-insensitive elastic substrate and microcrack-tunable conductive layer. Furthermore, the highly elastic amine-based polymer-modified polydimethylsiloxane substrate without obvious hysteresis endows our SDUS sensor with a rapid response time (2.33 ms) to external stimuli. The accurate detection of the radial pulse, joint motion, and vocal cord vibration proves the capability of SDUS sensor for healthcare monitoring and human-machine communications.**

**Keywords:** flexible strain sensor, microcrack, mechanophysiological signal monitoring, ultrahigh sensitivity, wide working range

## INTRODUCTION

Flexible strain sensors have drawn increasing attention for healthcare monitoring, daily activity tracking, and human-robotics communication [1–5]. A myriad of strain sensors based on various sensing mechanisms including resistance [6], capacitance [7,8], piezoresistive [9], piezoelectric [10], and inductance [11,12] have been developed. To meet the growing demand for practical medical applications in variable harsh conditions, stretching-resistive strain sensors have been widely used due to their ease of manufacturing and integration, cost-effectiveness, and scalability [13–16]. In general, resistive strain sensors turn strain to raising resistance as a result of gradual breaking of conductive path. In order to effectively measure the subtle and dynamic mechanical signals, sensitivity becomes the crucial benchmark determining the function and accuracy of the strain sensors for medical scenarios. At present, crack-based resistive sensors have been widely fabricated to achieve high gauge factor (GF), which contributes to improvement of the sensitivity [17,18]. It is worth noting that resistor thermal noise, which is positively associated with resistance, also significantly influences the detection output [13,19]. Therefore, highly conductive materials such as metals, liquid metal, graphene, carbon nanotubes (CNTs), metallic nanoplates and nanowires (NWs) are often used to construct conductive materials [20–22].

However, most sensing materials with superior conductivity have undesired mechanical flexibility, thus suffering a high risk of failure once subjected to severe deformation. To overcome the trade-off between ultrahigh sensitivity and wide working range, researchers incorporate different conductive nanomaterials to construct foam-shaped sensors or porous devices containing either a random distribution of multiscale pores or serpentine structures, which undesirably increase the device thickness and batch difference [23–26]. For real applications, long-term conformability and sustainability of the sensors are critical, requiring the sensors to be thin enough and highly reversible. To meet this practical demand, crack-based film sensors remain the potential candidate because of intrinsic high sensitivity and ease of fabrication with an ultralow thickness (typically below tens of microns) [27–29]. However, conventional crack-based sensors are short of wide working range due to rapid in-plane crack extension and propagation under concentrated stress [19,30,31]. The abrupt and unexpected mechanical response leads to thorough cracks transversely across the conductive layer, which in return terminates the conductance and damages the reversibility of sensors when subjected to large strain. Hence, controlling crack propagation and elongation under various strains remains a great challenge for building reversible strain sensors with both ultrahigh sensitivity and a wide working range.

[1] School of Biomedical Engineering and Informatics, Nanjing Medical University, Nanjing 211166, China
[2] Nanjing Drum Tower Hospital, The Affiliated Hospital of Nanjing University Medical School, Nanjing 210008, China
[3] School of Materials and Engineering, Nanjing Institute of Technology, Nanjing 211167, China
[4] The Affiliated Eye Hospital of Nanjing Medical University, Nanjing 210029, China
[5] Jiangsu Key Laboratory of Xenotransplantation, Nanjing Medical University, Nanjing 211166, China
[†] These authors contributed equally to this work.
[*] Corresponding author (email: hubenhui@njmu.edu.cn)

  

In this article, we propose a stress-deconcentrated ultrasensitive strain (SDUS) sensor that possesses an ultrahigh sensitivity (GF up to $2.3 \times 10^6$), wide working range (0%–50%) as well as rapid response to external stimuli (2.33 ms). Our SDUS sensor overcomes the trade-off between high sensitivity and wide working range by incorporating a notch-insensitive elastomer and a metal NW-based conductive layer consolidated with CNT-based intensifiers and dopamine (DA)-derived additives. Briefly, in the entangled conductive network, metal NWs with superb conductivity construct the main pathway for electron transmission and single-wall CNTs (SWCNTs) serve as conductive bypasses to bridge and densify the network, which is further intensified by polydopamine (PDA) with plentiful hydrogen bonds. Unlike the conventional crack-based resistive strain sensor which abruptly generates thorough cracks across the conductive film, the formation of microcracks of our SDUS sensor is prohibited and delayed to ~10% strain due to stress dissipation in the uniform conductive network. When the fractures occur and microcracks are detectable under larger strains, the consolidated conductive layer can effectively resist the extension of microcracks, preventing the termination of electrical conductivity. The microcracks propagate in a limited length and exhibit a distribution of high density and uniform orientation, which has substantially improved the mechanical robustness of the conductive network. Compared with conventional crack-based strain sensors which work in a relatively narrow working range (<2%), our sensor can maintain a significantly extended sensing range without sacrificing the sensitivity, broadening the application in various scenarios such as pulse wave monitoring, joint motion detection and speech recognition.

## EXPERIMENTAL SECTION

### Materials

Carboxylated SWCNTs (diameter = 30–50 nm, length = 0.5–2 μm) were purchased from Xianfeng nanotechnology Co., Ltd. Silver nitrate ($AgNO_3$), DA hydrochloride, polyvinylpyrrolidone (PVP, $M_w$ 360k), polyvinylpyrrolidone ($M_w$ 40k), copper chloride dihydrate ($CuCl_2{\cdot}2H_2O$), and ethylene glycol (EG) were obtained from Aladdin biochemical technology Co., Ltd. Ethoxylated polyethyleneimine (PEIE), chloroauric acid ($HAuCl_4$), sodium hydroxide (NaOH), ascorbic acid (AA), 1*H*,1*H*,2*H*,2*H*-perfluorooctyltrichlorosilane and sodium sulfite ($NaSO_3$) were purchased from Sigma-Aldrich. Polydimethylsiloxane (PDMS, Sylgard 184) monomer and cure agent were supplied by Dow chemical company.

### Preparation of Ag NWs

Ag NWs were prepared according to reported polyol-mediated processes [32]. In brief, 380 mg of PVP ($M_w$ 360k) was added to 130 mL of EG and pre-heated at 175°C under magnetic stirring (500 r $min^{-1}$). After PVP was completely dissolved, 800 μL of $CuCl_2$ solution (4 mmol $L^{-1}$) was added. After 10 min, a solution of $AgNO_3$ (484 mg in 30 mL EG) was added with a rate of 3 mL $min^{-1}$. When the addition was finished, the magnetic stirring was stopped, and the preparation reaction continued for 30 min. The dispersion of prepared Ag NWs was added into deionized water at a volume ratio of 1:4 and washed multiple times to remove extra PVP. Finally, the prepared Ag NWs were centrifuged and dried at 60°C for 12 h.

### Preparation of Au@Ag NWs

In brief, 8.4 mL of 0.2 mol $L^{-1}$ NaOH solution, 1.4 mL of 0.25 mol $L^{-1}$ $HAuCl_4$ solution, and 105 mL of 0.01 mol $L^{-1}$ $NaSO_3$ solution were added into 165 mL deionized water as Au growth solution. Then 100 mg of the prepared Ag NWs were added into 320 mL deionized water with ultrasonic dispersion. Seventy milliliter of 5 wt% PVP ($M_w$ 40k) solution, 14 mL of 0.5 mol $L^{-1}$ AA solution, 14 mL of 0.5 mol $L^{-1}$ NaOH solution, and 3.5 mL 0.5 mol $L^{-1}$ $Na_2SO_3$ solution were added in turn. After being well mixed, the Au growth solution was added and heated at 60°C for 12 h. Finally, the Au-coated Ag NWs (Au@Ag NWs) were collected, washed multiple times with deionized water and ethanol, and then dried at 60°C for 12 h. The diameter of Au@Ag NWs is 200 nm and the average length is about 10 μm (Fig. S1).

### Fabrication of the SUDS sensor

Carboxylated SWCNTs (5 mg) and DA (1 mg) were added into 10 mL of Tris-HCl solution (10 mmol $L^{-1}$, pH 8.5). After ultrasound dispersion for 2 h, the mixture was stirred for 24 h, and SWCNT suspension was obtained, where the DA had self-polymerized on the SWCNTs' surface to form PDA. Five hundred microgram of the prepared Au@Ag NWs was added into 1 mL of deionized water and ultrasonically dispersed. The conductive mixture was prepared *via* mixing the SWCNT suspension and Au@Ag NWs dispersion at a weight ratio of 1:10. The precursor of substrates was prepared by mixing PDMS monomer, cure agent, and PEIE at a weight ratio of 10:1:0.02 and spin-coating on the plastic plates at 1000 r $min^{-1}$ for 2 min. After curing under 60°C for 1 h, the semi-cured PDMS films were obtained with a thickness of 20 μm. Semi-cured PDMS surface was attached by a mask (rectangular hollow, 0.2 cm × 0.8 cm) and treated with oxygen plasma at 50 W for 5 min. The conductive mixture (10 μL) was dropped on the treated semi-cured PDMS surface and dried at room temperature for 12 h (Fig. S2). The sample was preloaded 1000 times under 0%–50% strain to reach a saturated initial resistance (157.74 Ω) for the fabrication of SDUS sensor. The control samples were prepared without PDA (Au@Ag NWs-SWCNTs, fabricated by SWCNTs and Au@Ag NWs at a weight ratio of 1:10, $C_{CNT\text{-}COOH}$ = 0.5 mg $mL^{-1}$, $C_{Au}$ = 5 mg $mL^{-1}$) or carboxylated SWCNTs (Au@Ag NWs-PDA, fabricated by PDA and Au@Ag NWs at a weight ratio of 1:50, $C_{DA}$ = 0.1 mg $mL^{-1}$, $C_{Au}$ = 5 mg $mL^{-1}$). The plastic plates and masks were treated with 1*H*,1*H*,2*H*,2*H*-perfluorooctyltrichlorosilane which contributed to the separation of PDMS substrates and plastic plates.

### Characterizations and measurements

The morphology of the conductive layer was observed on a field-emission scanning electron microscope (FE-SEM, JSM-7900F JOEL). The microcrack distribution and the dynamic extension with different strains were captured by a metallographic microscope (VTSE3-600 VIHENT).

The tensile tests at a range of 0%–50% strain, frequency response tests at a frequency range of 0.125–1 Hz for under 15% strain, cyclic tensile test at a strain ranging from 5% to 25%, and stability test of 1000 load-unload cycles at a strain of 50% were measured using a Criterion Electromechanical Test System (C42.503, MTS) at a tensile speed of 10 mm $min^{-1}$ and a Keithley 2450 source meter. Current-voltage (*I*-*V*) curves under strains of 0%, 1%, 5%, 10%, 30%, and 50% were collected using

  

the Keithley 2450 source meter with the applied voltage from −1 to 1 V. Response time experiment of the sensor was carried out with the Keithley 2450 source meter. The adhesion force of the PEIE-modified PDMS substrate was measured through a standard 90-degree peel-off approach using the Criterion Electromechanical Test System. The stress-strain curves of PDMS and PEIE-modified PDMS films were obtained on the Criterion Electromechanical Test system.

The radial pulse waves and electrocardiograph (ECG) signals were acquired using PowerLab (PL3516, AD Instruments) by placing a strain sensor on the tester wrist and two commercial Ag/AgCl electrodes on the left and right forearms, respectively. The speech recognition experiment was carried by attaching our sensor over the larynx and the resistance changes were collected using PowerLab. The recorded speech signals were treated with time-frequency analysis.

## RESULTS AND DISCUSSION

### Solution processing-based fabrication and sensing mechanism

We designed the SDUS sensor (Fig. 1a) by coating a mixed solution of the Au@Ag NWs, carboxylated SWCNTs and PDA on a flexible PDMS-based substrate. The ultrasoft substrate was prepared by adding an amine-based polymer (PEIE) into the PDMS precursor and cross-linker, which significantly decreased Young's modulus of the unmodified PDMS (1.77 MPa, Fig. S3) to 69.03 kPa by providing a heterogeneous crosslinked network [33]. Thus, the PEIE-modified PDMS substrate (m-PDMS) provides a conformal contact between the SDUS sensor and human skin (~25 kPa). In addition, the adhesion force of m-PDMS to porcine skin was measured *via* peel-off experiments (Fig. S4), providing a mechanically robust interface against delamination as large deformation induced by human motion. Moreover, the nearly superposed stretching and releasing curve of m-PDMS in the 0%–100% strain range indicates its outstanding recoverability (Fig. S5), as well as a low level of energy consumption when the strain signal is transmitted from the substrate to conductive layer, hence allowing a real-time response to deformation without mechanical hysteresis.

The conductive layer was prepared by polyol-mediated Au@Ag NWs and a PDA-modified CNT dispersion. By utilizing the self-polymerization of DA on carboxylated SWCNTs' surface, SWCNTs were uniformly dispersed in Tris-HCl solution (10 mmol $L^{-1}$, pH 8.5), which can be attributed to the offset of the van der Waals attraction between nanotubes [34]. In the conductive network constituted by nanofiber combination, Au@Ag NWs provide a primary conductive path for electron transmission and SWCNTs act as network densifiers that bridge the gaps between the NWs. Finally, the SDUS sensor was fabricated by drop-casting conductive solution on the oxygen plasma-treated semi-cured m-PDMS substrate, where the conductive material is uniformly deposited on the substrate and the coffee ring effect is suppressed by high aspect-ratio micrometre-sized Au@Ag NWs induced loose packing on the air-water interface [35]. As the tensile force is applied, microcrack propagation in the uniform film without gradient structure gives rise to the resistance change of our SDUS sensor [36]. More importantly, the adhesiveness of semi-cured m-PDMS and abundant hydrogen bonds between the substrate and conductive layer enhance the bonding force within the layers [37]. Specifically, interfacial PDA serves as junctional molecules whose hydroxyl and amino groups interact with the sulphite ligands of Au@Ag NWs and the carboxyl group of SWCNTs to form hydrogen bonds (Fig. 1b), which is advantageous for cohesiveness in the entangled conductive network. It also benefits the integration of functional conductive layer and oxygen plasma-treated substrate since the strong hydrogen bonds hold the layers together. As the tensile stress is applied, SWCNTs provide abundant conductive sites which allow the electrons to be transported between Au@Ag NWs and SWCNTs. Meanwhile, PDA prevents the debonding of the conductive layer from the m-PDMS substrate, as well as unexpected early electrical failure

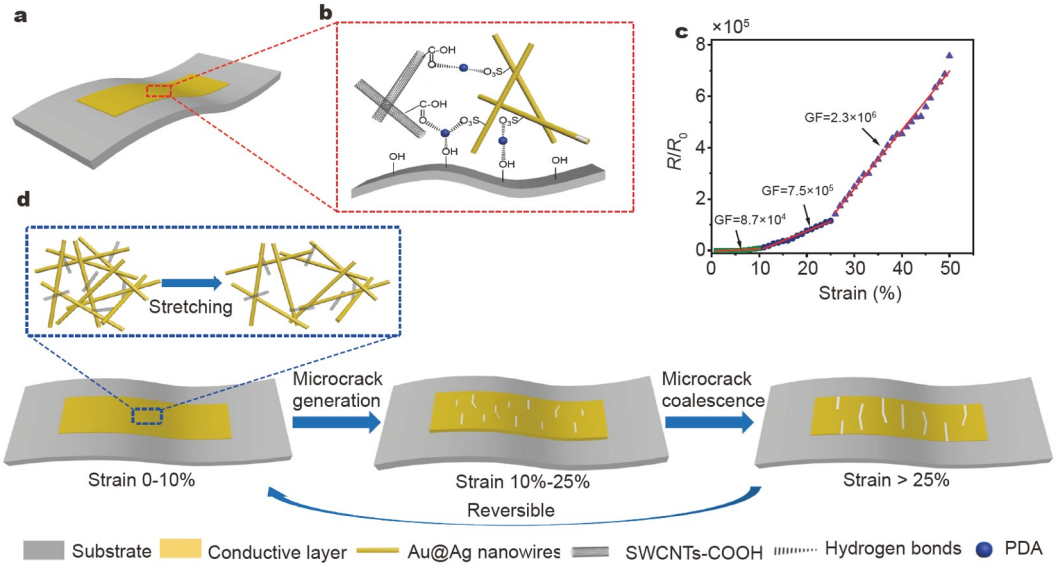


**Figure 1** Design and working mechanism of our SDUS sensor. (a) Schematic of the flexible strain sensor with the PDMS substrate and entangled conductive layer. (b) Illustration for the interaction of the Au@Ag NWs, carboxylated SWCNTs, PDA and substrate. (c) The resistance change of our SDUS sensor under different strains. (d) The illustration for a typical process of tensile stress response which includes microcrack prohibition, generation, and coalescence of the sensor.

  

induced by crack extension in the conductive layer, significantly improving the mechanical robustness.

To study the effect of PDA and SWCNTs on the sensitivity and sensing range of the SDUS sensor, we performed a tensile test on three sample groups and quantified the sensitivity with the GF defined as $(\Delta R/R_0)/\varepsilon$, where $\Delta R$ is the relative resistance change, $\varepsilon$ is the applied strain and $R_0$ is the saturated initial resistance after 1000 cycles of stretching ($R_0$ = 157.74 Ω) [38]. We observe that the SDUS sensor has three distinct stages of linear response to the applied stress (Fig. 1c), which correspond to the different sensing mechanisms in Fig. 1d. Initially, the SDUS sensor displays a moderate sensitivity with GF of $8.7 \times 10^4$ when the strain is below about 10%. At this stage, the resistance remains modest in the SDUS sensor and Au@Ag NWs-PDA sample, since PDA-provided hydrogen bonds inhibit the occurrence of microcracks in the conductive network (Fig. 1c and Fig. S6). The resistance increase of the SDUS sensor is ascribed to the sparsification of connection between conductive nanofibers (Fig. S7). By contrast, in the control sample without doping of PDA (Au@Ag NWs-SWCNTs sample), we observe a much larger resistance change at this stage (Fig. S6, blue curve), which can be attributed to the early formation of cracks without PDA inhibition. As larger strain is loaded (~10%–25%), microcracks form in the SDUS sensor with a dentate margin (SEM images in Fig. S8). The propagation of microcracks results in a significantly increased resistance, which in turn improves the sensitivity with an enlarged GF of $7.5 \times 10^5$. As the strain reaches around 25%, gradually emerging microcracks evolve into much longer cracks as coalescence between adjacent microcracks occurs, abruptly attenuating the electrical conductivity. The crack coalescence results in a surge of resistance change and the GF further increases to $2.3 \times 10^6$ while a tensile strain is between ~25% and 50%. Moreover, the working range of our sensor could be up to ~50% because PDA/SWCNTs dopants consolidate the conductive network, effectively inhibiting the stress concentration and perturbing the generation of thorough cracks. Apart from the ultrahigh sensitivity throughout the three sensing stages induced by a modified crack-based mechanism, our sensor exhibits a slow increase in resistance change over a larger strain range. Throughout the whole process, the sparsification of connection between conductive nanofibers contributes to the initially moderate change and major resistance change of the full working range is attributed to microcrack propagation, which can be further divided into the confined microcrack growth before coalescence and an accelerated extension of microcracks after coalescence.

**Quantitative analysis of microcrack distribution**

To reveal the underlying mechanism that contributes to the sensing characteristics of the SDUS sensor, we quantitatively investigated the microcrack distribution and the dynamic extension. The widespread distribution of cracks is established at a larger strain of 20% in our sensor with an average crack area of ~230.54 ± 12.54 μm$^2$ (Fig. S9, Fig. 2a). However, in the Au@Ag NWs-SWCNTs control sample, the crack area at a lower strain of 15% is ~1253.79 ± 74.43 μm$^2$, which is much larger than the crack area in the SDUS sample, suggesting that the PDA dopant strongly inhibits the occurrence of cracks (Fig. S10). Meanwhile, another control sample without doping of SWCNTs (the Au@Ag NWs-PDA sample) tends to form a sparse crack distribution in contrast to the dense arrangement of microcracks in SDUS sensor, which indicates that the SWCNTs can effectively deconcentrate the stress of conductive layer (Fig. S11). Thus, the presence of both SWCNTs and PDA contributes to the con-

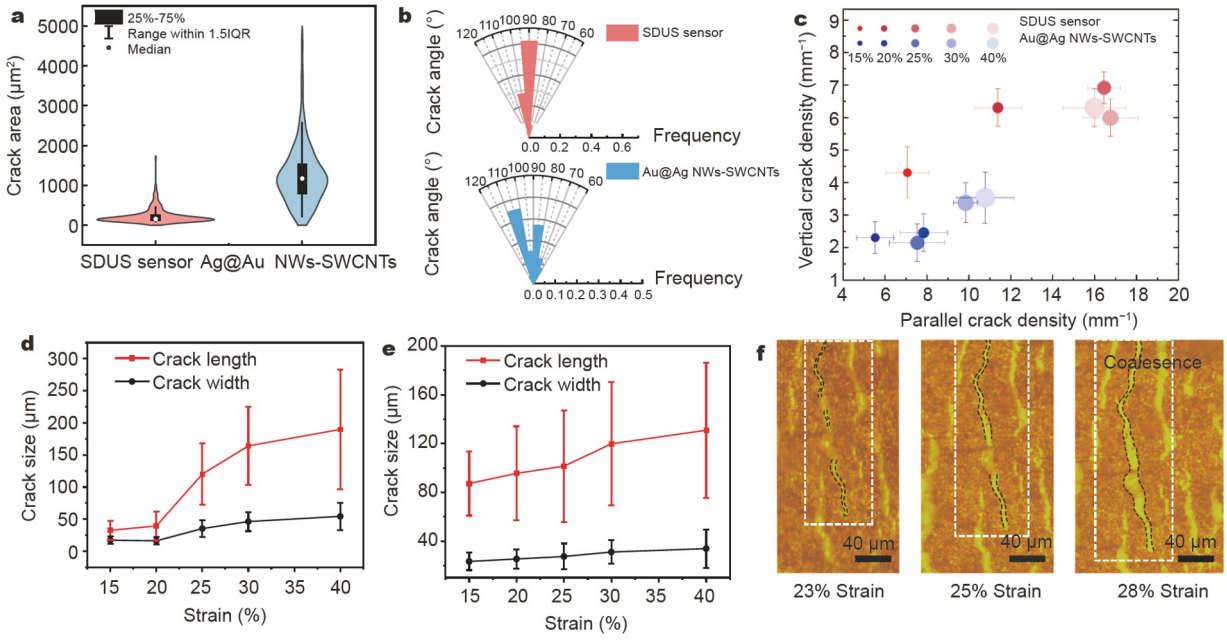


**Figure 2** Quantitative analysis of microcrack distribution and dynamic extension of our SDUS sensor. (a) Overall distribution of crack area as widespread cracks in SDUS sensor and Au@Ag NWs-SWCNTs sensor at 20% and 15% strain, respectively. (b) Crack angle to strain direction of SDUS sensor and Au@Ag NWs-SWCNTs sensor distributed in various frequencies. (c) Statistics of crack densities in parallel and vertical directions to strain of SDUS sensor and Au@Ag NWs-SWCNTs sensor under different strains of 15%, 20%, 25%, 30% and 40%. Data are shown as mean ± standard deviation of measured crack numbers at each strain. (d, e) Crack lengths and widths of SDUS sensor (d) and Au@Ag NWs-SWCNTs sensor (e) under different strains of 15%, 20%, 25%, 30% and 40%. Data are shown as mean ± standard deviation of measured crack numbers at each strain. (f) Metallographic microscopy images of a typical process of crack coalescence in SDUS sensor from 23% strain to 28% strain.

  

solidation of the conductive network, whereby the high-aspect-ratio conductive SWCNTs facilitate the electron transmitting in the primary conductive pathway and PDA molecules function as junctional units to provide reliable connection between conductive components with hydrogen bonding. As a result of the uniformly consolidated conductive network, our sensor exhibits the dominant distribution of perpendicular microcracks (Fig. 2b), contributing to the cyclic stability. In contrast, Au@Ag NWs-SWCNTs sample tends to yield irregular cracks of random size and orientation, inducing undesirable performance in terms of batch consistency and electrical reversibility.

We depicted the overall distribution by calculating the crack densities in vertical and parallel directions to tensile strain (Fig. 2c). The crack density of our sensor is much larger for all working range (strain 15%, 20%, 25%, 30% and 40%) in both directions, compared with Au@Ag NWs-SWCNTs sample. It is noteworthy that crack density of SDUS sensor exhibits a significant increase from 15% to 25% strain (7.07 and 16.45 $mm^{-1}$, parallel), while there is only a slight fluctuation of crack density as more strain is applied, indicating a saturated crack number above 25% strain. We further investigated the variation in crack size of our SUDS sensor and Au@Ag NWs-SWCNTs sample and illustrate the distinct crack propagation pattern in Fig. 2d, e. In the stress-deconcentrated network induced by widespread hydrogen bonds, the SDUS sensor tends to form much shorter and narrower cracks than the crack size of Au@Ag NWs-SWCNTs sample within 20% strain. Moreover, the crack length and width of SDUS sensor increase abruptly at 25% strain and henceforth maintain a continuous increase. For our SDUS sensor, the dramatic increment of crack length under around 25% strain originates from crack coalescence (Fig. 2f), which significantly impedes the conductive pathway and results in an abrupt increase in the resistance change curve. In sum, the high sensitivity and wide working range are ascribed to a dense and length-limited crack distribution on the stress-deconcentrated conductive layer.

**Electromechanical properties**

To investigate the sensing reliability of the SDUS sensor as a flexible strain sensor, we evaluated the electromechanical properties in Fig. 3. In the *I-V* test (Fig. 3a), the current increases linearly with the applied voltage from −1 to 1 V. The linear relationship between current and voltage signifies a typical Ohmic behavior of our sensor under strains of 1%, 5%, 10%, 30%, and 50% [39]. In addition, the suitability of the strain sensor to detect high-frequency signals is depicted by the response time, which is the period required by the resistance of a sensor to change from the previous value to a final state at the applied strain. By applying a steplike loading/unloading cycle, the swift-response curve demonstrates a rapid rising and falling response time of 2.33 and 2.34 ms, respectively (Fig. 3b), allowing a real-time response to high-frequency deformation signals. The PEIE additive substantially reduces the Young's modulus of PDMS without sacrificing its capability of high elasticity (Fig. S12).

To investigate the stability of the strain sensor under various working conditions, cyclic loading-unloading tests with a frequency range of 0.125–1 Hz were carried out on our SDUS sensor under a fixed maximum strain of 15%. As shown in Fig. 3c, our sensor possesses a frequency-independent property and symmetric loading-unloading rate. The sensor also shows high cyclic reliability at various strains ranging from 5% to 25% (Fig. 3d). We performed 1000 cycles/11,000 s cyclic tests with a maximum strain of 50% on our sensor (Fig. 3e), verifying the

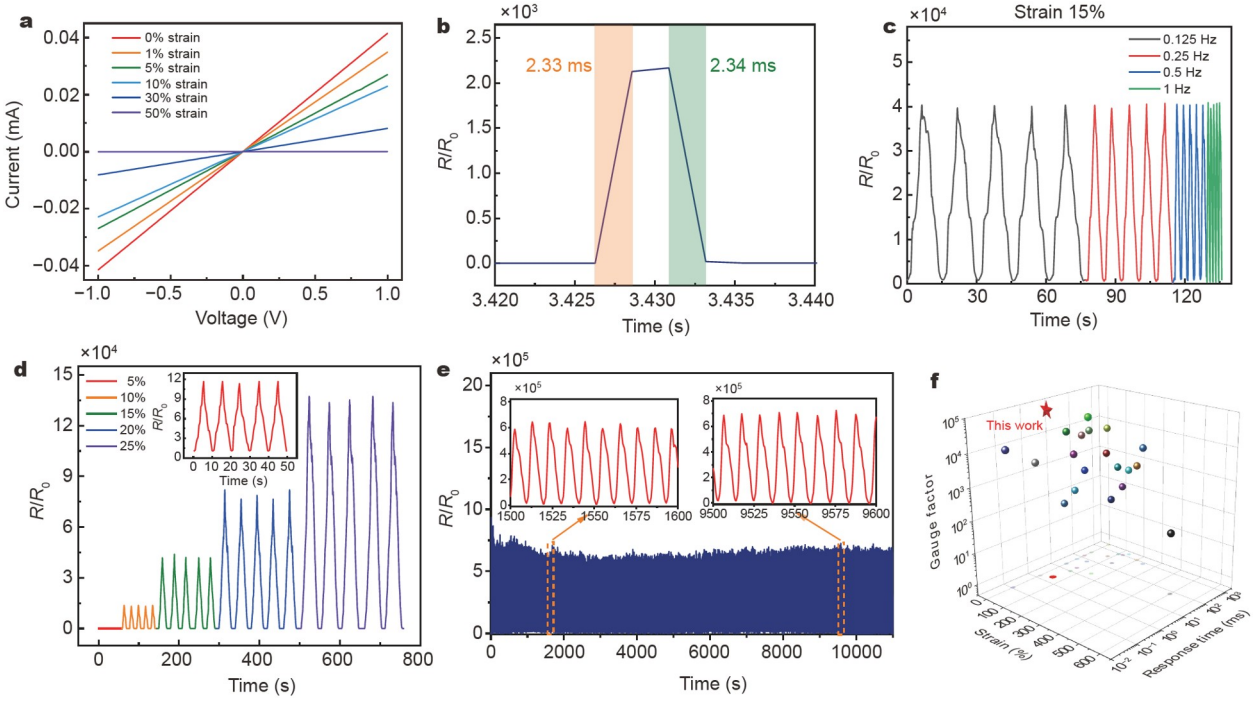


**Figure 3** Electromechanical properties of our SUDS sensor. (a) The *I-V* curves of our SUDS sensor under various strains. (b) Time response of the strain sensor. (c, d) The relative resistance change of our SUDS sensor under stretching-releasing cycles at different frequencies (c) and strains (d). (e) Cyclic stability of our SUDS sensor in 1000 stretching cycles/11,000 s at 50% strain. (f) Gauge factor, working range and response time comparison of reported strain sensors and our SUDS sensor.

  

excellent durability of SDUS sensor during long-term deformation monitoring. In the zoomed-in 100 s cycles at the early and late periods, we observed a slight variation in the initial resistance value and peak due to the dentate margin of microcracks. Specifically, although microcracks are uniformly distributed in the stress-deconcentrated conductive layer, the jagged crack margin prevents the sensor from smoothly recovering to its original state after stress release.

Compared with the reported crack-based strain sensors, our SUDS sensor has advantages in sensitivity, response time and working range (Fig. 3f, Table S1). In previous reports, carbonized natural or synthetic fibers-based strain sensors usually exhibit a balanced performance in GFs (35–14,000), the response time (10–200 ms) and working range (64%–500%) [40–42]. For strain sensors based on CNTs wrapped in elastic polymeric substrates, the sensitivity is significantly higher with GFs in a range of 425–42,300 [43–48], even though some of the sensors have a delayed response to strain [45,47]. Strain distribution control by introducing microstructure to conductive fibers or films is also adopted as a potential strategy to improve the working range of strain sensors (120%–135%), while those sensors still have limited GFs (100 and 337.8) [49,50]. Some bio-inspired sensors utilize brittle materials like metal films and rigid plastic to generate cracks and are generally sensitive to strain (GFs in the range of 50–6000). However, the performances of these sensors are severely limited by their narrow working range (<2%) [2,17,51,52]. By contrast, our SDUS sensor possesses a superior sensitivity, a millisecond response time and a relatively wide working range, enabling the device to monitor of various biomechanical signals.

**Mechanophysiological signal monitoring**

To verify the feasibility of our sensor as a wearable device for capturing subtle mechanophysiological signals, our strain sensor was applied in the continuous monitoring of radial pulse (Fig. 4a). By attaching our sensor to the tester's wrist, we observed a repeatable and consistent pulse waveform of the same tester during the continuous monitoring (Fig. 4a), which indicates a real-time response to the subtle mechanical deformation and long-term stability of the sensor. Particularly, three typical peaks of percussion wave ($P_1$), tidal wave ($P_2$), and dicrotic wave can be accurately recorded (Fig. 4b), illustrating its high sensitivity. Thus, we can extract the radial augmentation index ($r_{AI} = P_2/P_1$, generally ranging from 0.5 to 1.3) from the characteristic

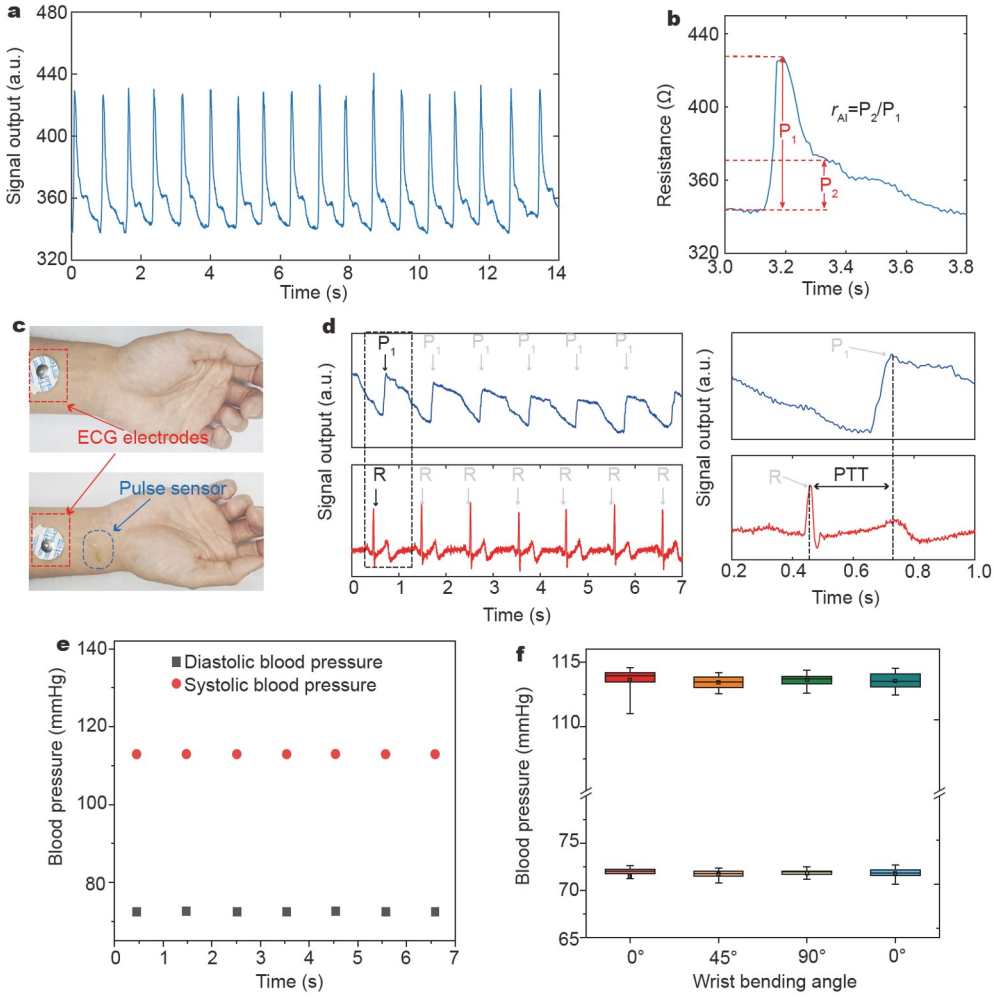


**Figure 4** Demonstration of radial pulse waveforms recording and blood pressure measurement using our SUDS sensor. (a) Resistance changes of SUDS sensor induced by radial pulse. (b) Enlarged view showing the pulse waveforms. (c) Photograph of the SUDS sensor and commercial Ag/AgCl electrodes attaching to the wrist. (d) Recorded concurrent ECG signals and radial pulse waveforms (left) and indicated PTT (right). (e) Calculated DBP and SBP according to PTT. (f) Box plots of the blood pressures at different wrist bending angles of 0°, 45°, and 90°, respectively.

  

pattern of radial pulse peaks to assess the radial stiffness [53], whereby a larger value of $r_{AI}$ implies a high risk of cardiovascular disease (Fig. 4b). Furthermore, by adhering two commercial Ag/AgCl electrodes on the forearms coupled with our sensor (Fig. 4c), we can obtain blood pressure from the time interval between the R-peak of the electrocardiogram signals and the $P_1$ peak of the pulse waveform in the same cardiac cycle (Fig. 4d, left), which is defined as pulse transit time (PTT) (Fig. 4d, right). PTT reflects the velocity at which arterial pulse travels between proximal and distal arteries and is highly correlated to blood pressure. The calculation for diastolic blood pressure (DBP) and systolic blood pressure (SBP) conforms to the following equations [54]:

$$\mathrm{DBP} = \frac{\mathrm{SBP}_0}{3} + \frac{2\mathrm{DBP}_0}{3} + A\ln\left(\frac{\mathrm{PTT}_0}{\mathrm{PTT}}\right) - \frac{(\mathrm{SBP}_0 - \mathrm{DBP}_0)}{3}\frac{\mathrm{PTT}_0^2}{\mathrm{PTT}^2}, \quad (1)$$

$$\mathrm{SBP} = \mathrm{DBP} + (\mathrm{SBP}_0 - \mathrm{DBP}_0)\frac{\mathrm{PTT}_0^2}{\mathrm{PTT}^2}, \quad (2)$$

where $\mathrm{SBP}_0$ and $\mathrm{DBP}_0$ are measured values of commercial sphygmomanometers for calibration, which initialize the monitoring sensor for the conversion of measured time delay to absolute blood pressure value. $A$ is a subject-related coefficient, and $\mathrm{PTT}_0$ is the initial PTT for the first recording cycle. The continuously measured DBP and SBP values with our sensor are in accordance with the results ($\mathrm{SBP}_0$ = 113 mmHg, $\mathrm{DBP}_0$ = 72 mmHg) from a commercial sphygmomanometer (Fig. 4e). To demonstrate the anti-interference capability of our sensor under various wrist movements during blood pressure monitoring, we measured the blood pressure with different preloads by varying the wrist bending angle (0°, 45°, and 90°) and observed consistent results. The high sensitivity, well-performed linearity and stability endow our sensor with the capability of providing reliable physiological information for health management and auxiliary diagnosis. Benefiting from the wide working range of ~50%, our SDUS sensor is applicable for measuring both small and large joint motions, such as knuckle movements (Fig. S13). The obvious variation of relative resistance is corresponded to different bending degrees of the index finger joint (30°, 60°, and 90°), indicating the potential for gesture recognition and robotics interaction.

To evaluate the capability of detecting feeble deformation at high frequencies, we utilized our sensor as an acoustic sensor by attaching it over the larynx to monitor vocal cord vibration (Fig. S14). First, we used our sensor for recognizing monosyllabic pronunciations like English letters "N", "J", "M" and "U", which were recorded as featured waveforms of relative resistance change with different amplitudes and durations (Fig. S15). Furthermore, we compared the waveform and spectrogram of our sensor and a reference microphone when the tester pronounced the disyllabic words "sensor" and "nanowire". As illustrated in Fig. S16, the output signal of our sensor exhibits an enhanced temporal and frequency resolution. After that, we simulated a noisy environment by manually adding white noise (~50 dB) as the tester consecutively pronounced "carbon nanowire sensor". It is obvious that the pronunciation signals recorded by our sensor have a lower level of baseline noise, while the results of the reference microphone are indistinguishable and submerged in plentiful noise (Fig. 5a, b). In detail, Fig. 5c proposes the local and intuitive information of baseline noise signals from 2.00 to 2.01 s, which is quantitively analyzed in Fig. 5d. Our sensor has a significantly lower max-

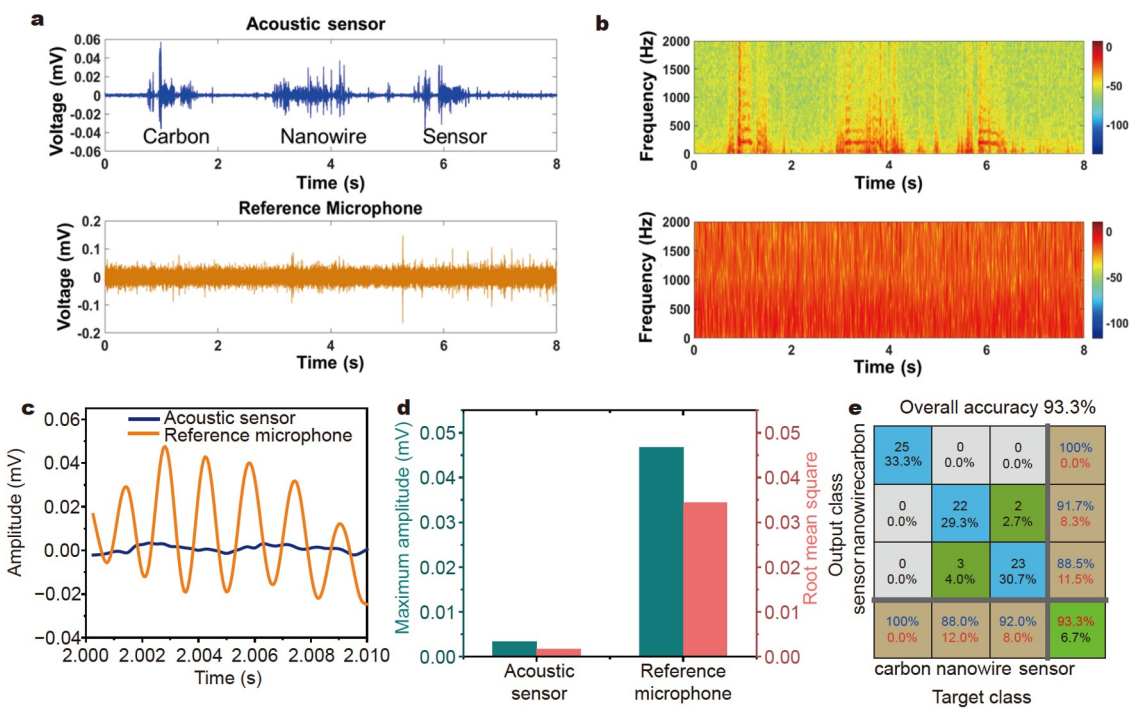


**Figure 5** Application of our SUDS sensor for anti-interference speech recording. (a, b) Comparison of the phonation of "carbon, nanowire, sensor" recorded by the acoustic sensor (a) and reference microphone (b). The recordings were made in a noisy environment. (c) Enlarged view showing the comparison of baseline amplitude of the recorded phonation signals using the acoustic sensor and reference microphone from 2.00 to 2.01 s. (d) The maximum amplitude and root mean square of the baseline. (e) Confusion matrix for the classification accuracy of each word pronunciations.

  

imum amplitude and root mean square (RMS) of 3.35 and 1.68 μV, respectively, compared with those of the reference microphone at 46.77 and 34.33 μV, indicating a superior capability of our sensor for capturing feeble strain and its anti-interference ability. By combining artificial intelligence with a digital signal process tool, our sensor achieves a reliable classification of the disyllabic word pronunciations (overall accuracy = 93.3%) and is promising in the application for speech recognition (Fig. 5e).

## CONCLUSION

In conclusion, we reported a mechanically robust and fracture-resilient resistive strain sensor based on manipulated initiation and propagation of microcracks. The superior sensitivity (GF up to $2.3 \times 10^6$), wide working range (0%–50%) and rapid response time (2.33 ms) broaden the applicability of our sensor as wearable electronics in various scenarios, such as pulse wave monitoring, gesture detection and speech recognition. We have adopted an adhesive and notch-insensitive elastomer matrix to obtain a conformable and highly reversible substrate. More importantly, we have studied and verified the effect of SWCNTs and PDA on consolidation of the conductive network and substantial modulation of microcrack growth, whereby the crack generation is prohibited at early stretching stage (strain < 10%) and microcrack propagation is confined within a limited size under larger strains (~10%–25%). In addition, we have conducted a quantitative analysis to depict the aligned and dense microcrack distribution which contributes to the wide working range and high stability of the SDUS sensor. Our sensor is anticipated to provide augmented perception of biomechanical monitoring and be robustly applied in human-robotics communications and clinical healthcare.

**Received 2 January 2022; accepted 3 February 2022; published online 17 March 2022**


1 Wang J, Wang C, Cai P, *et al.* Artificial sense technology: Emulating and extending biological senses. ACS Nano, 2021, 15: 18671–18678
2 Han Z, Liu L, Zhang J, *et al.* High-performance flexible strain sensor with bio-inspired crack arrays. Nanoscale, 2018, 10: 15178–15186
3 Zhang R, Jiang J, Wu W. Scalably nanomanufactured atomically thin materials-based wearable health sensors. Small Struct, 2022, 3: 2100120
4 Cui Z, Wang W, Guo L, *et al.* Haptically quantifying Young's modulus of soft materials using a self-locked stretchable strain sensor. Adv Mater, 2021, 33: 2104078
5 Mo F, Wang Z, Jiang R, *et al.* Energy-dissipative dual-crosslinked hydrogels for dynamically super-tough sensors. Sci China Mater, 2021, 64: 2764–2776
6 Shi L, Li Z, Chen M, *et al.* Quantum effect-based flexible and transparent pressure sensors with ultrahigh sensitivity and sensing density. Nat Commun, 2020, 11: 3529
7 Mannsfeld SCB, Tee BCK, Stoltenberg RM, *et al.* Highly sensitive flexible pressure sensors with microstructured rubber dielectric layers. Nat Mater, 2010, 9: 859–864
8 Sharma S, Chhetry A, Zhang S, *et al.* Hydrogen-bond-triggered hybrid nanofibrous membrane-based wearable pressure sensor with ultrahigh sensitivity over a broad pressure range. ACS Nano, 2021, 15: 4380–4393
9 Cheng Y, Ma Y, Li L, *et al.* Bioinspired microspines for a high-performance spray $Ti_3C_2T_x$ MXene-based piezoresistive sensor. ACS Nano, 2020, 14: 2145–2155
10 Cheng S, Han S, Cao Z, *et al.* Wearable and ultrasensitive strain sensor based on high-quality GaN pn junction microwire arrays. Small, 2020, 16: 1907461
11 Kouhani MHM, Wu J, Tavakoli A, *et al.* Wireless, passive strain sensor in a doughnut-shaped contact lens for continuous non-invasive self-monitoring of intraocular pressure. Lab Chip, 2020, 20: 332–342
12 Wu Y, Liu Y, Zhou Y, *et al.* A skin-inspired tactile sensor for smart prosthetics. Sci Robot, 2018, 3: eaat0429
13 Hong W, Jiang C, Qin M, *et al.* Self-adaptive cardiac optogenetics device based on negative stretching-resistive strain sensor. Sci Adv, 2021, 7: eabj4273
14 Li Y, Liu Y, Bhuiyan SRA, *et al.* Printed strain sensors for on-skin electronics. Small Struct, 2022, 3: 2100131
15 Bai J, Wang R, Ju M, *et al.* Facile preparation and high performance of wearable strain sensors based on ionically cross-linked composite hydrogels. Sci China Mater, 2021, 64: 942–952
16 Jia Y, Chen W, Ye C, *et al.* Controllable formation of periodic wrinkles in Marangoni-driven self-assembled graphene film for sensitive strain detection. Sci China Mater, 2020, 63: 1983–1992
17 Kang D, Pikhitsa PV, Choi YW, *et al.* Ultrasensitive mechanical crack-based sensor inspired by the spider sensory system. Nature, 2014, 516: 222–226
18 Li H, Tan Z, Yuan L, *et al.* Eggshell-inspired membrane—Shell strategy for simultaneously improving the sensitivity and detection range of strain sensors. Sci China Mater, 2021, 64: 717–726
19 Cho C, Kang P, Taqieddin A, *et al.* Strain-resilient electrical functionality in thin-film metal electrodes using two-dimensional interlayers. Nat Electron, 2021, 4: 126–133
20 Xu J, Wang Z, You J, *et al.* Polymerization of moldable self-healing hydrogel with liquid metal nanodroplets for flexible strain-sensing devices. Chem Eng J, 2020, 392: 123788
21 Luo Z, Li X, Li Q, *et al.* *In situ* dynamic manipulation of graphene strain sensor with drastically sensing performance enhancement. Adv Electron Mater, 2020, 6: 2000269
22 Ma Z, Huang Q, Xu Q, *et al.* Permeable superelastic liquid-metal fibre mat enables biocompatible and monolithic stretchable electronics. Nat Mater, 2021, 20: 859–868
23 Xu M, Li F, Zhang Z, *et al.* Stretchable and multifunctional strain sensors based on 3D graphene foams for active and adaptive tactile imaging. Sci China Mater, 2019, 62: 555–565
24 Zhang L, Li H, Lai X, *et al.* Three-dimensional binary-conductive-network silver nanowires@thiolated graphene foam-based room-temperature self-healable strain sensor for human motion detection. ACS Appl Mater Interfaces, 2020, 12: 44360–44370
25 Cai JH, Li J, Chen XD, *et al.* Multifunctional polydimethylsiloxane foam with multi-walled carbon nanotube and thermo-expandable microsphere for temperature sensing, microwave shielding and piezoresistive sensor. Chem Eng J, 2020, 393: 124805
26 Sun Y, Zhang Z, Zhou Y, *et al.* Wearable strain sensor based on double-layer graphene fabrics for real-time, continuous acquirement of human pulse signal in daily activities. Adv Mater Technol, 2021, 6: 2001071
27 Kim KH, Hong SK, Ha SH, *et al.* Enhancement of linearity range of stretchable ultrasensitive metal crack strain sensor *via* superaligned carbon nanotube-based strain engineering. Mater Horiz, 2020, 7: 2662–2672
28 Liu C, Li M, Lu B, *et al.* High-sensitivity crack-based flexible strain sensor with dual hydrogen bond-assisted structure for monitoring tiny human motions and writing behavior. Org Electron, 2021, 88: 105977
29 Wang YF, Sekine T, Takeda Y, *et al.* Printed strain sensor with high sensitivity and wide working range using a novel brittle-stretchable conductive network. ACS Appl Mater Interfaces, 2020, 12: 35282–35290
30 Yang H, Xiao X, Li Z, *et al.* Wireless $Ti_3C_2T_x$ MXene strain sensor with ultrahigh sensitivity and designated working windows for soft exoskeletons. ACS Nano, 2020, 14: 11860–11875
31 Sun Z, Yang S, Zhao P, *et al.* Skin-like ultrasensitive strain sensor for full-range detection of human health monitoring. ACS Appl Mater Interfaces, 2020, 12: 13287–13295
32 Choi S, Han SI, Jung D, *et al.* Highly conductive, stretchable and biocompatible Ag-Au core-sheath nanowire composite for wearable and implantable bioelectronics. Nat Nanotech, 2018, 13: 1048–1056
33 Jeong SH, Zhang S, Hjort K, *et al.* PDMS-based elastomer tuned soft, stretchable, and sticky for epidermal electronics. Adv Mater, 2016, 28: 5830–5836


  

34 Ling Y, Li W, Wang B, *et al.* Epoxy resin reinforced with nanothin polydopamine-coated carbon nanotubes: A study of the interfacial polymer layer thickness. RSC Adv, 2016, 6: 31037–31045
35 Yunker PJ, Still T, Lohr MA, *et al.* Suppression of the coffee-ring effect by shape-dependent capillary interactions. Nature, 2011, 476: 308–311
36 Liu Z, Qi D, Guo P, *et al.* Thickness-gradient films for high gauge factor stretchable strain sensors. Adv Mater, 2015, 27: 6230–6237
37 Ding J, Fu S, Zhang R, *et al.* Graphene—Vertically aligned carbon nanotube hybrid on PDMS as stretchable electrodes. Nanotechnology, 2017, 28: 465302
38 Dinh Le TS, An J, Huang Y, *et al.* Ultrasensitive anti-interference voice recognition by bio-inspired skin-attachable self-cleaning acoustic sensors. ACS Nano, 2019, 13: 13293–13303
39 Wang H, Zhou R, Li D, *et al.* High-performance foam-shaped strain sensor based on carbon nanotubes and $Ti_3C_2T_x$ MXene for the monitoring of human activities. ACS Nano, 2021, 15: 9690–9700
40 Wang C, Li X, Gao E, *et al.* Carbonized silk fabric for ultrastretchable, highly sensitive, and wearable strain sensors. Adv Mater, 2016, 28: 6640–6648
41 Zhong W, Liu C, Xiang C, *et al.* Continuously producible ultrasensitive wearable strain sensor assembled with three-dimensional interpenetrating Ag nanowires/polyolefin elastomer nanofibrous composite yarn. ACS Appl Mater Interfaces, 2017, 9: 42058–42066
42 Zhang M, Wang C, Wang H, *et al.* Carbonized cotton fabric for high-performance wearable strain sensors. Adv Funct Mater, 2017, 27: 1604795
43 Cai Y, Shen J, Ge G, *et al.* Stretchable $Ti_3C_2T_x$ MXene/carbon nanotube composite based strain sensor with ultrahigh sensitivity and tunable sensing range. ACS Nano, 2018, 12: 56–62
44 Gao Y, Fang X, Tan J, *et al.* Highly sensitive strain sensors based on fragmentized carbon nanotube/polydimethylsiloxane composites. Nanotechnology, 2018, 29: 235501
45 He T, Lin C, Shi L, *et al.* Through-layer buckle wavelength-gradient design for the coupling of high sensitivity and stretchability in a single strain sensor. ACS Appl Mater Interfaces, 2018, 10: 9653–9662
46 Xin Y, Zhou J, Xu X, *et al.* Laser-engraved carbon nanotube paper for instilling high sensitivity, high stretchability, and high linearity in strain sensors. Nanoscale, 2017, 9: 10897–10905
47 Zhou J, Xu X, Xin Y, *et al.* Coaxial thermoplastic elastomer-wrapped carbon nanotube fibers for deformable and wearable strain sensors. Adv Funct Mater, 2018, 28: 1705591
48 Lee J, Pyo S, Kwon DS, *et al.* Ultrasensitive strain sensor based on separation of overlapped carbon nanotubes. Small, 2019, 15: 1805120
49 Liu Z, Qi D, Hu G, *et al.* Surface strain redistribution on structured microfibers to enhance sensitivity of fiber-shaped stretchable strain sensors. Adv Mater, 2018, 30: 1704229
50 Chen H, Lv L, Zhang J, *et al.* Enhanced stretchable and sensitive strain sensor *via* controlled strain distribution. Nanomaterials, 2020, 10: 218
51 Wang C, Zhao J, Ma C, *et al.* Detection of non-joint areas tiny strain and anti-interference voice recognition by micro-cracked metal thin film. Nano Energy, 2017, 34: 578–585
52 Luo C, Jia J, Gong Y, *et al.* Highly sensitive, durable, and multifunctional sensor inspired by a spider. ACS Appl Mater Interfaces, 2017, 9: 19955–19962
53 Fu Y, Zhao S, Wang L, *et al.* A wearable sensor using structured silver-particle reinforced PDMS for radial arterial pulse wave monitoring. Adv Healthcare Mater, 2019, 8: 1900633
54 Xu Y, Sun B, Ling Y, *et al.* Multiscale porous elastomer substrates for multifunctional on-skin electronics with passive-cooling capabilities. Proc Natl Acad Sci USA, 2020, 117: 205–213


**Acknowledgements** This work was supported by the National Key Research and Development Program of China (2019YFA0210104), the National Natural Science Foundation of China (81971701), the Natural Science Foundation of Jiangsu Province (BK20201352), and the Program of Jiangsu Specially-Appointed Professor.

**Author contributions** Yang Y, Tang W, Wang J designed and performed the experiments, and wrote the paper; Hu B proposed the concept and supervised this study. All authors contributed to the general discussion and revision of the manuscript.

**Conflict of interest** The authors declare that they have no conflict of interest.

**Supplementary information** Supporting data are available in the online version of the paper.

**Yizhuo Yang** is currently an undergraduate student at Nanjing Medical University (NJMU). Her research interests mainly focus on flexible strain sensors and their application in biomechanical signal monitoring.

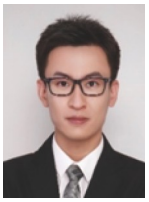

**Benhui Hu** received his PhD degree from Nanyang Technological University in Singapore. He started an independent research career as a full professor at the School of Biomedical Engineering and Informatics, NJMU in 2018, and served as the deputy director of the Department of Biomedical Engineering, NJMU. His research focuses on implantable/wearable diagnostic and therapeutic flexible devices, which are used in real-time multimodal monitoring and boosted tissue repair.

## 氢键控制断裂韧性的应力分散超灵敏应变传感器用于稳定的生物力监测

杨仪卓[1†], 唐文杰[1†], 王金毅[1,2†], 刘瑞清[1], 杨平[3], 陈士晟[1], 袁月辉[1], 徐景丰[1], 任雪洋[1], 余善成[1], 吴昊[1], 周云帆[4], 翟磊莉[4], 邵小东[4], 陈泽楠[1], 胡本慧[1,4,5*]

**摘要** 近年来, 柔性应变传感器的迅速发展, 拓宽了其在各种机械生理信号监测中的应用范围. 在各种应变传感器中, 基于裂纹的应变传感器由于其高灵敏度, 在监测微小的机械变形方面越来越受到重视. 然而, 由于导电传感层中裂纹的早期产生和快速扩展导致裂纹传感器工作范围狭窄, 限制了其在监测较大生物力学变形中的应用. 本研究通过引入缺口不敏感的弹性基底和可调微裂纹的导电层, 开发了具有超高灵敏度(应变系数高达$2.3 \times 10^6$)和宽工作范围(0%–50%)的应力分散超灵敏应变(SDUS)传感器. 此外, 高弹性胺基聚合物修饰的聚二甲基硅氧烷衬底没有明显的迟滞, 使SDUS传感器对外界刺激能够快速响应(响应时间2.33 ms). 通过对桡动脉脉搏、关节运动和声带振动的精确检测, SDUS传感器在医疗健康监测和人机通信方面的能力得到了验证.

  